JOURNAL OF GEOPHYSICAL RESEARCH, VOL. 105, NO. B8, PAGES 19,289–19,303, AUGUST 10, 2000

Dilatancy, compaction, and failure mode in Solnhofen limestone

Patrick Baud

Department of Geosciences, State University of New York at Stony Brook

Alexandre Schubnel

Laboratoire de Géologie, Département Terre, Atmosphère et Océan, Ecole Normale Supérieure, Paris

Teng-fong Wong

Department of Geosciences, State University of New York at Stony Brook

Abstract. Failure mode is intimately related to porosity change, and whether deformation occurs in conjunction with dilatation or compaction has important implications on fluid transport processes. Laboratory studies on the inelastic and failure behavior of carbonate rocks have focused on the very porous and compact end-members. In this study, experiments were conducted on the Solnhofen limestone of intermediate porosity to investigate the interplay of dilatancy and shear compaction in controlling the brittle-ductile transition. Hydrostatic and triaxial compression experiments were conducted on nominally dry samples at confining pressures up to 435 MPa. Two conclusions can be drawn from our new data. First, shear-enhanced compaction can be appreciable in a relatively compact rock. The compactive yield behavior of Solnhofen limestone samples (with initial porosities as low as 3%) is phenomenologically similar to that of carbonate rocks, sandstone, and granular materials with porosities up to 40%. Second, compactive cataclastic flow is commonly observed to be a transient phenomenon, in that the failure mode evolves with increasing strain to dilatant cataclastic flow and ultimately shear localization. It is therefore inappropriate to view stress-induced compaction and dilatancy as mutually exclusive processes, especially when large strains are involved as in many geological settings. Several theoretical models were employed to interpret the micromechanics of the brittle-ductile transition. The laboratory data on the onset of shear-enhanced compaction are in reasonable agreement with *Curran and Carroll's* [1979] plastic pore collapse model. In the transitional regime, the *Stroh* [1957] model for microcrack nucleation due to dislocation pileup can be used to analyze the transition from shear-enhanced compaction to dilatant cataclastic flow. In the brittle faulting regime the wing crack model provides a consistent description of the effect of grain size on the onset of dilatancy and brittle faulting.

1. Introduction

It is important to have a fundamental understanding of the mechanics of the brittle-ductile transition in many geologic problems. The deformation mechanisms operative on scales ranging from the microscopic to macroscopic have profound influence on the microstructure preserved in naturally deformed rocks, the limits on the state of stress in the lithosphere, the spatiotemporal evolution of stress and deformation during the earthquake cycle, and the coupling of crustal deformation and fluid transport. It is now recognized that the brittle-ductile transition is associated with a broad regime of complex deformation and failure mode. The mechanics of the transition is sensitively dependent on extrinsic variables (that include confining and pore pressures, temperature, strain rate, and fluid chemistry) as well as intrinsic variables (that include modal composition, grain size, and porosity).

Previous studies have demonstrated that porosity change and failure mode are intimately related. On one hand, dilatancy is universally observed as a precursor to the inception of shear localization in the brittle faulting regime [*Brace*, 1978]. On the other hand, plastic flow (associated with crystal plasticity and diffusive mass transfer) does not involve any volumetric change [*Paterson*, 1978]. In the transitional regime of cataclastic flow (manifested by homogeneously distributed microcracking) the scenario is more complicated since the pore space may dilate or compact in response to an applied stress field.

In relatively porous silicate rocks [e.g., *Handin and Hager*, 1957; *Hadizadeh and Rutter*, 1983; *Shimada*, 1986] a transition of the failure mode from brittle fracture to cataclastic flow can be induced at room temperature by an increase in pressure only. In the cataclastic flow regime the pore space undergoes significant inelastic compaction while the rock strain hardens [*Edmond and Paterson*, 1972]. The

Paper number 2000JB900133.
0148-0227/00/2000JB900133$09.00

transition pressure decreases with increasing porosity and grain size [*Wong et al.*, 1997]. In contrast, relatively compact granite, gabbro, dunite, and eclogite remain in the brittle fracture regime when tested at room temperature and confining pressures up to 3 GPa [*Shimada et al.*, 1983]. It seems that even at the maximum confining pressure accessible in the laboratory, elevated temperatures are necessary to activate crystal plasticity processes so that silicate rocks of relatively low porosity can undergo the transition to cataclastic and ultimately crystal plastic flow [*Tullis and Yund*, 1992; *Hirth and Tullis*, 1994].

In calcite rocks the brittle-ductile transition has somewhat different attributes from silicate rocks. Limestones and marbles, even the ones with very low porosity like the Carrara marble, undergo the brittle to plastic transition at room temperature for confining pressures accessible in the laboratory [*Robertson*, 1955; *Paterson*, 1958; *Heard*, 1960; *Rutter*, 1974]. This is probably due to the fact that calcite requires relatively low shear stresses to initiate mechanical twinning and dislocation slip even at room temperature [*Turner et al.*, 1954; *Griggs et al.*, 1960]. The transition occurs at a pressure that decreases with increasing grain size [*Fredrich et al.*, 1990]. In Carrara marble, appreciable dilatancy occurs even when shear localization is inhibited and the sample strain hardens [*Fredrich et al.*, 1989; *Fischer and Paterson*, 1989]. That dilatancy occurs while the compact marble undergoes cataclastic flow suggests that the deformation mechanisms are different from those in the compactive type of cataclastic flow observed in a porous sandstone or chalk [*Teufel et al.*, 1991].

Previous experimental studies of the brittle-ductile transition have focused on the two end-members with relatively low or high porosities that are associated with purely dilatant or compactive cataclastic flow. In a rock with porosity intermediate between these two end-members, strain hardening and cataclastic flow are expected to arise from the complex interplay of dilatant and compactive deformation mechanisms. In this transitional regime it is unlikely that compaction and dilatancy can be considered as mutually exclusive deformation processes, especially when large strains are involved as in many geological field settings. Indeed, the interplay of compaction and dilatancy is a central feature in many constitutive models for porous geomaterials [e.g., *Fossum et al.*, 1995].

In an attempt to elucidate the interplay and partitioning of dilatancy and compaction we conducted detailed measurements of the stress and strain, as well as their influence on the failure mode of the Solnhofen limestone (with an initial porosity of 3%). Although many aspects of the brittle-ductile transition and creep behavior in this rock have been studied [*Robertson*, 1955; *Heard*, 1960; *Byerlee*, 1968; *Edmond and Paterson*, 1972; *Rutter*, 1972; *Schmid et al.*, 1977; *Fredrich et al.*, 1990; *Renner and Rummel*, 1996; *Fisher and Paterson*, 1989], to our knowledge the compactive behavior was not investigated systematically. Motivated by the laboratory data, we have developed theoretical models (involving various modes of grain-scale fracture and crystal plasticity) to analyze the micromechanics. We also discuss the implications of the micromechanical models on the effect of porosity and grain size on the brittle-ductile transition in calcite and silicate rocks.

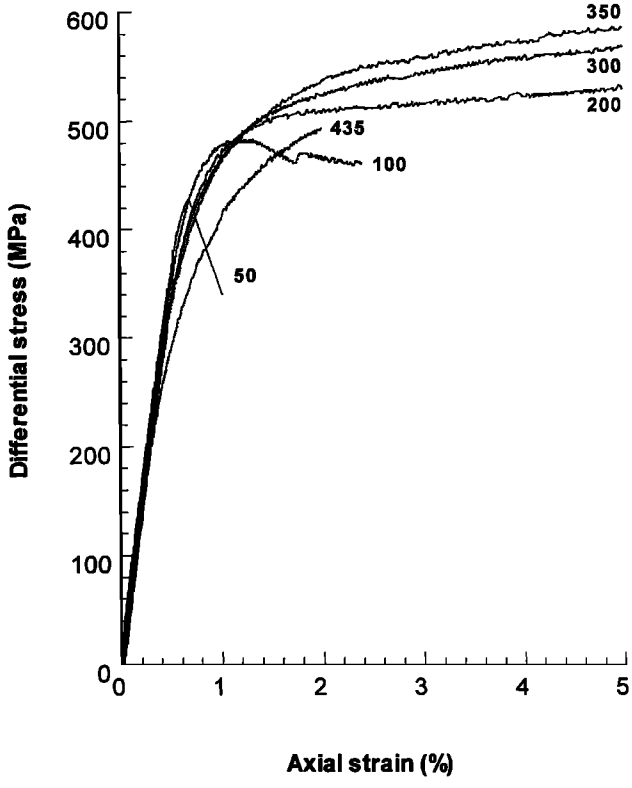

Figure 2. Representative mechanical data for selected triaxial compression experiments. Differential stress is plotted versus axial strain.

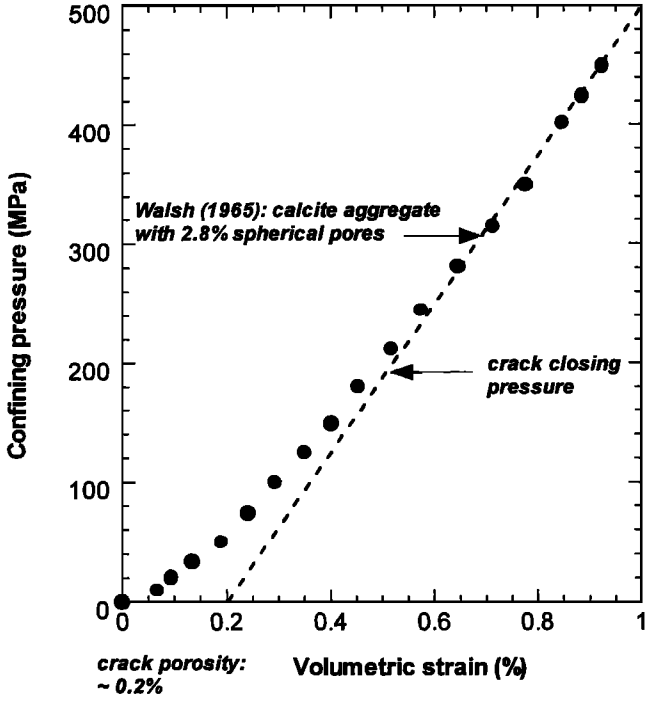

Figure 1. Mechanical data for a hydrostatic experiment up to 450 MPa. Volumetric strain is plotted versus confining pressure. The linear part of the curve is fitted by linear regression. Closing crack pressure and microcrack porosity are indicated.

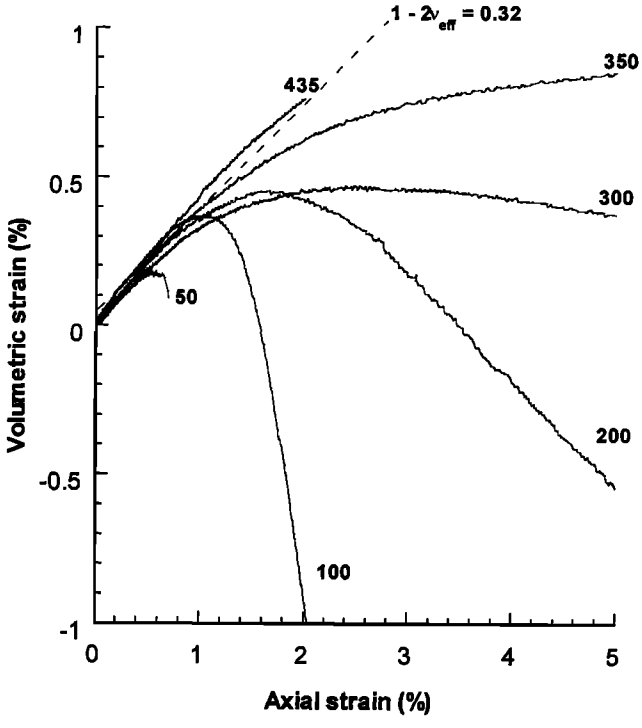

Figure 3. Representative mechanical data for selected triaxial compression experiments. Axial strain is plotted versus volumetric strain (for the nonhydrostatic part of the experiments). The confining pressure (in MPa) is indicated on each curve. For reference, the linear portion is fitted with a line that corresponds to a Poisson's ratio of 0.34.

2. Mechanical Data

2.1. Sample Material and Preparation

Solnhofen limestone is composed of 99.9% of calcite. We determined the total porosity of each of our samples that were cored from the same block. After measuring the weight and the volume of the sample we calculated its porosity (assuming that it was entirely composed of calcite). We found that the total porosity ranges from 2.7% to 3.3%, with an arithmetic mean of 3.0%. Our block is less porous than samples used in most previous studies (with total porosities ranging from 3.7% to 5.9%), except for *Heard's* [1960] samples that had 1.7% of porosity. We also used the saturation technique to determine the interconnected porosities in selected samples, which were found to be ~1.5%, indicating that the limestone contains a large proportion of unconnected, vugular type of pores. We did not determine the average grain size, but it was reported to be ~5 μm in previous studies [*Robertson*, 1955; *Heard*, 1960; *Edmond and Paterson*, 1972; *Fredrich et al.*, 1990; *Renner and Rummel*, 1996; *Fisher and Paterson*, 1989; *Rutter*, 1972].

Rock samples were cored to a diameter of 18.1 mm and cut to a length of 38.1 mm. The samples were dried in vacuum at 80°C for several days. They were first jacketed with a thin copper foil, and heat-shrink polyolefine tubings were then used to separate the sample from confining pressure. The longitudinal and transverse strains were measured by electric resistance strain gauges (BHL Constantan foil FAE-50-12-S6 for measurements of strains up to 5%). A hydrostatic pressure of 50 MPa was first applied to each sample to "season" the copper jacket, and then the strain gauges were glued on the jacketed sample in orthogonal directions. The volumetric strain was calculated using the relation $\varepsilon_v = \varepsilon_{||} + 2\varepsilon_{\perp}$, where $\varepsilon_{||}$ and $\varepsilon_{\perp}$ are the strains measured in the axial and transverse directions, respectively. This formula neglects second-order contributions of strains to the volume change that may be appreciable at relatively large strains.

2.2. Experimental Procedure

The jacketed samples were stressed in the conventional triaxial configuration at room temperature. Kerosene was used as the confining medium. The experiments were performed at confining pressures ranging from 10 to 435 MPa. The axial load was measured with an external load cell with an accuracy of 1 kN. The displacement was measured outside the pressure vessel with a displacement transducer (DCDT) mounted between the moving piston and the fixed upper platen. The axial displacement was servo-controlled at a fixed rate (corresponding to a nominal strain rate of 1.3×10^{-5} s^{-1}).

The load, displacement, and strain gauge signals were acquired by a 14-bit A/D converter at a sampling rate of 1 s^{-1} with resolutions of 0.3 MPa, 1 μm and 10^{-5}, respectively. Owing to electrical noise and sample shortening, actual uncertainty in strain was 2×10^{-3} (when calculated from the DCDT signal) and 10^{-5} (when measured directly by the strain gauges). Acoustic emission (AE) recordings were available via a piezoelectric transducer (PZT-7, 5 mm diameter, 1 MHz

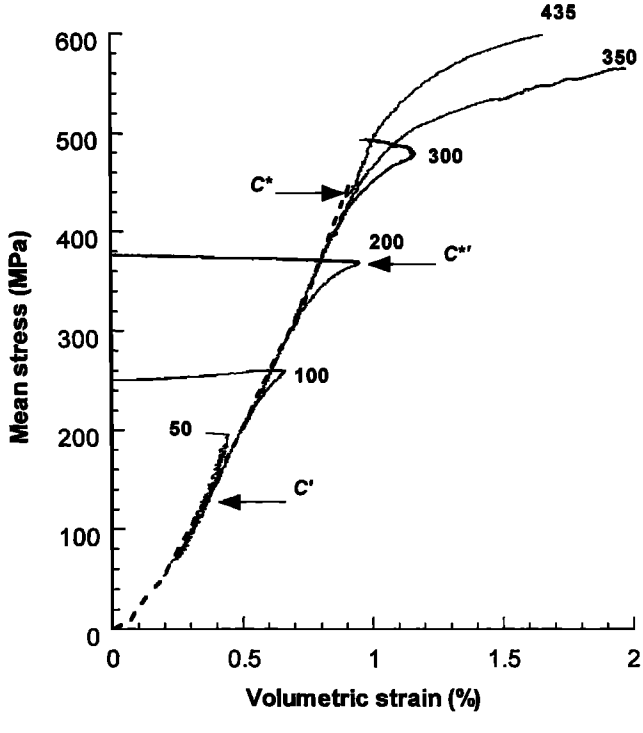

Figure 4. Representative mechanical data for selected triaxial compression experiments. Volumetric strain is plotted versus mean stress. The confining pressure (in MPa) is indicated on each curve. For reference, the hydrostat is shown as heavy dashed line. The critical stress states for dilatancy *C'*, onset of shear-enhanced compaction *C**, and transition from shear-enhanced compaction to dilatancy *C*'* are indicated by the arrows for experiments performed at confining pressures of 50, 300, and 200 MPa, respectively.

longitudinal resonant frequency) positioned on the flat surface of one of the end plugs. However, during all the series of experiments that we did, no significant AE activity was observed over the background noise of our laboratory. The AE data were not of use in this study.

2.3. Stress, Strain, and Porosity Change

We will adopt the convention that compressive stresses and compactive strains are positive, and we will denote the maximum and minimum (compressive) principal stresses by σ_1 and σ_3, respectively. Figure 1 shows the evolution of the volumetric strain for a hydrostatic experiment up to 450 MPa of confining pressure. The hydrostatic response was nonlinear up to a pressure of ~ 200 MPa, beyond which the stress-strain curve became linear with a slope corresponding to a compressibility of $\beta_{eff} = 1.6 \times 10^{-11}$ Pa^{-1}.

Figure 2 shows the differential stress ($\sigma_1 - \sigma_3$) as a function of axial strain in selected experiments conducted at confining pressures (σ_3) ranging from 50 to 435 MPa. Except for the experiment at the lowest confining pressure of 10 MPa, both the axial and radial strain data were acquired. The volumetric strain data from these experiments are plotted as a function of the axial strain in Figure 3 and versus the mean stress $(\sigma_1 + 2\sigma_3)/3$ in Figure 4. For reference, the hydrostat is also shown (as the dashed line) in Figure 4.

At confining pressures up to 50 MPa the mechanical response and failure mode are typical of the brittle faulting regime. The differential stress attained a peak, beyond which strain softening was observed (Figure 4). In some experiments the unstable failure resulted in breakage of the strain gages. The peak stress shows a positive correlation with the confining pressure and mean stress (Table 1), and the failed samples show macroscopic failure oriented at ~30° with respect to the σ_1 direction. As indicated for the experiment at confining pressure of 50 MPa, the onset of dilatancy C' can be identified on Figure 4 as the point where the volume of the triaxially compressed sample became greater than that of the hydrostatically compressed counterpart at the same mean stress. This implies that at stress levels beyond C' the deviatoric stress field induced the pore space to dilate. The differential stress level at C' showed a positive pressure dependence (Table 1).

At confining pressures $\sigma_3 \geq 350$ MPa the mechanical response and failure mode are typical of the compactive cataclastic flow regime. The slopes of the differential stress-axial strain curve were nonnegative (Figure 2), and the sample volume decreased monotonically with deformation up to a finite strain of 5% (Figure 3). Shear localization was not evident in the deformed samples. As shown in Figure 4, the triaxial curves for a given confining pressure coincided with the hydrostat up to a critical stress state (indicated by C^* for the data at 435 MPa confining pressure), beyond which there was an accelerated decrease in volume in comparison to the hydrostat. At stress levels beyond C^* the deviatoric stress field provided significant inelastic contribution to the compactive strain, and this phenomenon is referred to as "shear-enhanced compaction" [*Curran and Carroll*, 1979; *Wong et al.*, 1997]. The differential stress at C^* is negatively correlated with the confining pressure and mean stress (Table 1).

In the transitional regime (100 MPa $\leq \sigma_3 \leq$ 300 MPa) the evolution of volumetric strain showed three distinct stages (Figure 5). Initially, the triaxial and hydrostatic data for volumetric strain as function of mean stress coincide. The second stage was manifested by shear-enhanced compaction, with the onset marked by the critical stress state C^*. However, these samples in the transitional regime consistently switched from compaction to a third stage of dilation after they had undergone certain amount of strain hardening. As indicated in Figure 4 for the experiment at 200 MPa confining pressure, the critical stress state at the transition from compactive to dilatant cataclastic flow will be denoted by $C^{*\prime}$.

Visual examination of all the deformed samples from this transitional regime (up to the maximum axial strain of ~5%) did not reveal any signs of shear localization, even though a transient phase of strain softening was observed in the experiment at confining pressure of 100 MPa. While the differential stress at the onset of shear-enhanced compaction in this transitional regime shows a negative pressure dependence that is comparable to the C^* data for $\sigma_3 \geq 350$ MPa, the differential stress at $C^{*\prime}$ shows a slightly positive correlation with mean stress and confining pressure (Table 1).

3. Discussion

Our laboratory data have important implications in the interpretation of compactive and dilatant processes in the crust. However, quantitative extrapolations of the laboratory data to crustal settings would require a fundamental understanding of the micromechanics of the brittle-ductile transition, which cannot be formulated without a realistic

Table 1. Compilation of Mechanical Data for the Solnhofen Limestone

Confining Pressure, MPa	C' $\sigma_1 - \sigma_3$, MPa	C' $(\sigma_1 + 2\sigma_3)/3$, MPa	Peak Stress $\sigma_1 - \sigma_3$, MPa	Peak Stress $(\sigma_1 + 2\sigma_3)/3$, MPa	C^* $\sigma_1 - \sigma_3$, MPa	C^* $(\sigma_1 + 2\sigma_3)/3$, MPa	$C^{*\prime}$ $\sigma_1 - \sigma_3$, MPa	$C^{*\prime}$ $(\sigma_1 + 2\sigma_3)/3$, MPa
10	-	-	326	120	-	-	-	-
25	200	92	360	145	-	-	-	-
35	225.5	112	409	177	-	-	-	-
50	245	132	428	197	-	-	-	-
100	-	-	-	-	375	225	475	258
200	-	-	-	-	354	318	509	370
250	-	-	-	-	336	362	510	420
300	-	-	-	-	315	405	526	475
350	-	-	-	-	270	440	-	-
395	-	-	-	-	231	470	-	-
435	-	-	-	-	179	495	-	-

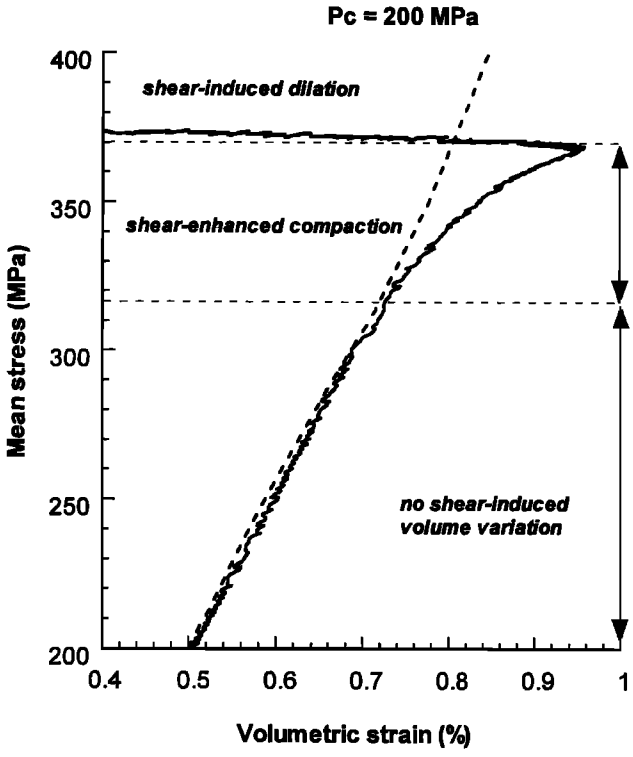

Figure 5. The mean stress is plotted as a function of volumetric strain for an experiment performed at 200 MPa of confining pressure. The sample showed compactive and dilatant behavior. For reference, the hydrostat is shown as heavy dashed line.

conception of the pore geometry and defect structure. We will first use the mechanical data to infer the pore structure of Solnhofen limestone and to develop theoretical models to analyze different stages of the brittle-ductile transition. Specifically, a wing crack model will be employed to analyze the development of dilatancy and brittle faulting, a plastic pore collapse model for shear-enhanced compaction, and a dislocation pileup model for the transition from shear-enhanced compaction to dilatancy. These models elucidate the damage mechanics as well as the important influences of porosity and grain size in the brittle-ductile transition.

3.1. Interplay of Compaction and Dilatancy During Cataclastic Flow

Recent studies have emphasized that there are fundamental differences in the mechanical and transport properties of compactive and dilatant types of cataclastic flow as observed in high- and low-porosity silicate rocks, respectively [*Wong et al.*, 1997; *Zhu and Wong*, 1997]. However, there have been a paucity of data for addressing the question: At what porosity will the transition from dilatant to compactive cataclastic flow occur? A value of ~5% was suggested by *Brace* [1978], and here we demonstrate that shear-enhanced compaction and pore collapse are readily observed in a limestone that has an initial porosity as low as 3% and pore size that is probably comparable to the average grain size (~5 μm).

This implies that pore collapse is a fairly common deformation process that can occur even in rocks considered to be relatively compact. However, it should be noted that such compactive deformation may be transient in nature. As mapped in the stress space (Figure 6), the yield stresses for shear-enhanced compaction in Solnhofen limestone are initially described by a compactive yield envelope with negative slope that expands with strain hardening, gradually evolving to a dilatant yield envelope with positive slope. Although it has not been explored systematically, this intriguing phenomenon of compaction as a transient precursor leading to dilatancy seems to be not very uncommon. In the literature, *Schock et al.* [1973] reported phenomenological behavior in the Lance sandstone (with 7.5% porosity) that is very similar to our observations for Solnhofen limestone. For comparison, we determined from their stress-strain curves values of C^*, $C^{*\prime}$, C', and brittle strength and plotted the data in Figure 7.

It is therefore inappropriate to view stress-induced compaction and dilatancy as mutually exclusive processes, especially when large strains are involved, as in many geological field settings. Our experiments were conducted up to a maximum axial strain of ~5%. It is conceivable that more complex behavior would occur if deformation was to develop to even larger strains. The brittle-ductile transition is associated with a broad spectrum of highly complex deformation mechanisms, failure modes, and fluid transport processes. While dilatant cataclastic flow may be a transient precursor for the inception of shear localization and brittle faulting, shear-enhanced compaction may also evolve to dilatant cataclasis. Extrapolation of our laboratory data to the temporal and spatial scales of geologic settings would require a fundamental understanding of the micromechanics of the brittle-ductile transition, which may involve the complex interplay of microcracking, crystal plasticity, and diffusive mass transfer processes in Solnhofen limestone.

3.2. Pore Structure of Solnhofen Limestone Inferred From Elastic Properties

Relevant micromechanical models cannot be formulated without a realistic conception of the pore geometry and defect structure. Many geometric attributes of the pore space can be inferred from the elastic behavior. According to *Walsh* [1965] the hydrostat in Figure 1 is characteristic of the response of a rock pore space made up of two types of cavities: microcracks of relatively low aspect ratios and relatively equant pores. The progressive closure of the microcracks under increasing pressure was manifested by the nonlinearity observed during initial pressurization. At and above a pressure of ~ 200 MPa the microcracks were closed and the hydrostat became linear. As shown in Figure 1, one can then use *Walsh's* [1965] analysis to infer that the microcrack porosity is ~0.2% for our Solnhofen limestone and that the aspect ratios of the microcracks are of the order of 10^{-3} or less.

The linear portion of the hydrostat represents the hydrostatic response of a rock with pore space made up of relatively equant pores, with a porosity of ~2.8% (equal to the difference between the total and microcrack porosity). Additional information on the pore geometry can be obtained by comparison of the elastic moduli with theoretical results for an elastic matrix embedded with dilute concentration of spherical pores [*Walsh*, 1965; *Walsh and Brace*, 1966]. With the Reuss assumption of uniform stress the effective compressibility β_{eff} for such an idealized porous material is linearly related to the porosity ϕ:

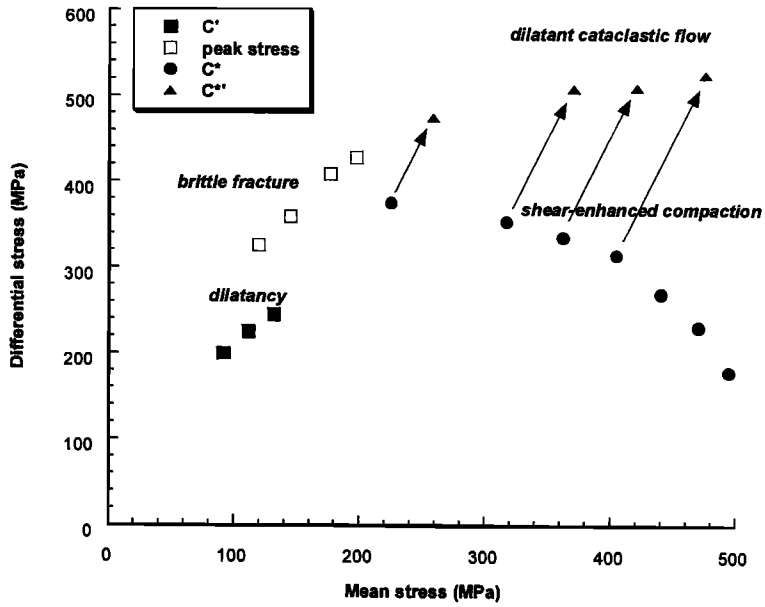

Figure 6. Stress states C', C^* and $C^{*\prime}$ and brittle strength are shown in the P-Q space for our Solnhofen limestone data. Three regimes of inelastic and failure modes can be identified: brittle fracture, dilatant cataclastic flow, and shear-enhanced compaction.

$$\frac{\beta_{eff}}{\beta} = 1 + \frac{3}{2}\frac{(1-\nu)}{(1-2\nu)}\frac{\phi}{1+\phi} \tag{1a}$$

where β and ν are the intrinsic compressibility and Poisson's ratio, respectively, of the solid (calcite) grain. The Reuss averages for the intrinsic elastic moduli of a calcite aggregate at 300 MPa pressure [*Simmons and Wang*, 1971] are $\beta = 1.379 \times 10^{-11}$ Pa^{-1} and $\nu = 0.335$. Assuming a porosity $\phi = 2.8\%$, equation (1a) gives an effective compressibility $\beta_{eff} = 1.5 \times 10^{-11}$ Pa^{-1} that is very close to our measured value of 1.6×10^{-11} Pa^{-1}.

The hydrostatic data therefore suggest that the Solnhofen limestone has ~0.2% of microcrack porosity and ~2.8% of quasi-spherical pores (Figure 8a). A similar conclusion is obtained if we consider the other elastic moduli. The theoretical value for the effective Poisson's ratio of an elastic matrix embedded with dilute concentration of spherical pores is [*Walsh and Brace*, 1966]

$$\frac{\nu_{eff}}{\nu} = 1 + \frac{3}{2}\frac{(1-\nu^2)(5\nu-1)}{(7-5\nu)}\phi. \tag{1b}$$

Substituting in $\nu = 0.335$ and $\phi = 2.8\%$, we have $\nu_{eff} = 0.34$. For comparison, the linearly elastic portion of the axial and volumetric strain data has a slope of $1 - 2\nu_{eff} = 0.32$ (Figure 3), which implies that the effective Poisson's ratio of the limestone (when all the microcracks has been closed) is given by $\nu_{eff} = 0.34$, in agreement with the model prediction.

3.3. Development of Dilatancy and Brittle Faulting: Wing Crack Growth and Coalescence

Dilatancy in brittle rock has been observed to arise from intragranular and intergranular cracking with a preferred orientation for propagation that is parallel to the maximum principal stress σ_1. In the strain softening stage, microcracking activity localizes along a macroscopic shear band [*Tapponier and Brace*, 1976; *Wong*, 1982; *Fredrich et al.*, 1989]. As shown in Figure 8b, a conceptual model widely used to analyze such micromechanical processes is the "sliding wing crack" [e.g., *Horii and Nemat-Nasser*, 1986; *Ashby and Sammis*, 1990; *Kemeny and Cook*, 1991]. The model considers the growth of "wing cracks" that initiate from tensile stress concentration at the tips of preexisting cracks undergoing frictional slip. The fracture mechanics is such that increasing the stress causes the wing crack to propagate along a curved path and ultimately reach a stable orientation parallel to the direction of σ_1. With the accumulation of such anisotropic damage distributed throughout the rock, it will ultimately attain a critical state at which the multiplicity of cracks coalesce to develop a shear band.

The sliding wing crack model considers sources of tensile stress concentration that are located at the tips of preexisting cracks (with initial length $2a$ and oriented at angle γ to σ_1). The applied stresses induce a shear traction on the crack plane, and if this resolved shear traction is sufficiently high to overcome the frictional resistance along the closed crack, frictional slip results in tensile stress concentrations at the two tips which may induce wing cracks to nucleate and extend out of the initial plane of the main sliding crack (Figure 8b). The driving force is characterized by the stress intensity factor K_I at the tip of the putative wing crack. With increased loading, it will attain the critical value K_{IC}, at which point a wing crack nucleates and propagates along a curved path to ultimately reach a stable orientation parallel to the direction of σ_1.

If the onset of dilatancy C' is identified with the initiation of wing cracks and if the rock is assumed to contain randomly oriented cracks, then the wing cracks should first nucleate from those sliding cracks oriented at $\gamma = 1/2\tan^{-1}(1/\mu)$, where μ is the frictional coefficient. The principal stresses at the onset of dilatancy are given by [*Cotterell and Rice*, 1980; *Horii and Nemat-Nasser*, 1986; *Ashby and Sammis*, 1990]

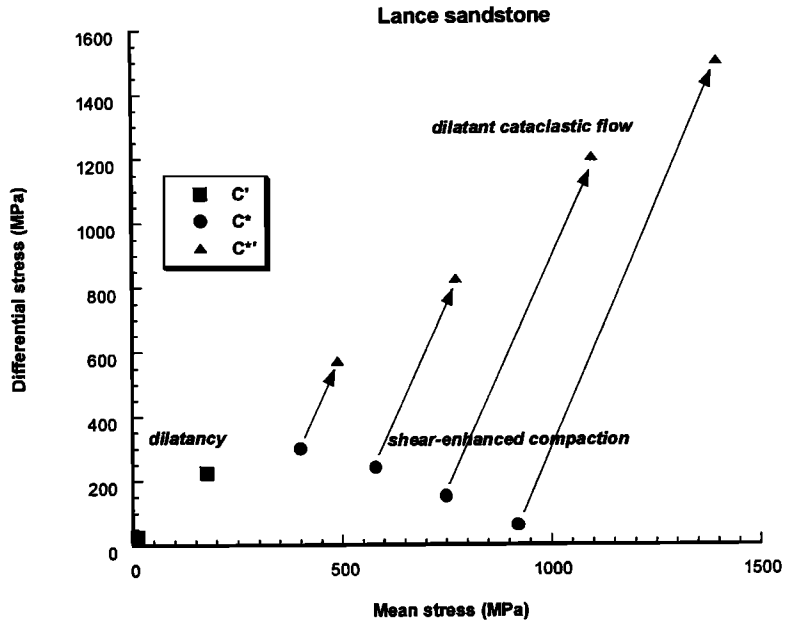

Figure 7. Stress states C', C^*, and $C^{*\prime}$ are shown in the P-Q space for Lance sandstone. The stress values were evaluated from data of *Schock et al.* [1973].

$$\sigma_1=\frac{\sqrt{1+\mu^2}+\mu}{\sqrt{1+\mu^2}-\mu}\sigma_3+\frac{\sqrt{3}}{\sqrt{1+\mu^2}-\mu}\frac{K_{IC}}{\sqrt{\pi a}}. \qquad (2)$$

To analyze the peak stress, we adopted *Ashby and Sammis'* [1990] two-dimensional (plane strain) model for mathematical convenience. The key damage parameter in this model is the crack density $D=\pi(l+a\cos\gamma)^2N_A$, where l is the length of the wing crack and N_A is the number of sliding cracks of uniform orientation γ per unit area initially present. Before wing cracks nucleate the length $l=0$ and therefore the initial damage is given by $D_0=\pi(a\cos\gamma)^2N_A$. With the progressive development of dilatancy the remotely applied principal stresses evolve with damage in accordance with equation (17) of *Ashby and Sammis* [1990], written here with our sign convention (compression is positive):

$$\sigma_1=\left[C_1+\frac{C_4(\sqrt{D/D_0}-1)}{1+\sqrt{\pi D_0}\dfrac{\sqrt{D/D_0}-1}{1-\sqrt{D}}}\right]\sigma_3$$

$$+\frac{\left(\sqrt{D/D_0}-1+0.1/\cos\gamma\right)^{1/2}}{1+\sqrt{\pi D_0}\dfrac{\sqrt{D/D_0}-1}{1-\sqrt{D}}}\frac{C_4}{\sqrt{\cos\gamma}}\frac{K_{IC}}{\sqrt{\pi a}}, \qquad (3)$$

where

$$C_1=(\sqrt{1+\mu^2}+\mu)/(\sqrt{1+\mu^2}-\mu)$$

and

$$C_4=\sqrt{30}\cos\gamma/(\sqrt{1+\mu^2}-\mu).$$

If one specifies the material parameters D_0, $K_{IC}/(\pi a)^{1/2}$, and μ, then the evolution of the principal stress σ_1 as a function of damage D at a fixed confining stress σ_3 can be calculated using equation (3). In the brittle faulting regime the stress attains a peak beyond which instability sets in.

Repeating the calculation for different values of fixed σ_3 allows one to map out the brittle failure envelope in the principal stress space. To a first approximation this failure envelope for the wing crack model [*Horii and Nemat-Nasser*, 1986; *Ashby and Sammis*, 1990; *Fredrich et al.*, 1990; *Kemeny and Cook*, 1991] can be described by a linear relation

$$\sigma_1=A(\mu,D_0)\sigma_3+B(\mu,D_0)K_{IC}/\sqrt{\pi a}. \qquad (4)$$

If triaxial compression data for the onset of dilatancy and peak stress follow the linear trends described by equations (2) and (4), then the slopes and intercepts of the two sets of stress data provide four constraints for inferring the three parameters D_0, $K_{IC}/(\pi a)^{1/2}$, and μ. These inferred parameters and the fit of our limestone data to equations (2) and (4) are shown in Figure 9. Our estimate of $\mu=0.53$ is close to *Ashby and Sammis'* [1990] estimate of 0.55 on the basis of *Heard's* [1960] data. However, our estimates of $K_{IC}/(\pi a)^{1/2}=97$ MPa and $D_0=0.25$ are higher than their values of $K_{IC}/(\pi a)^{1/2}=68$ MPa (corresponding to $K_{IC}=0.6$ MPa $m^{1/2}$ and $a=25$ μm) and $D_0=0.15$, respectively. *Heard* [1960] presented a limited set of peak stress data, and since he did not measure the volumetric strain, the onset of dilatancy cannot be determined from his data. *Ashby and Sammis* [1990] assumed that wing crack initiation in *Heard's* [1960] experiments was associated with the onset of nonlinearity in the stress-strain curves. In comparison, our estimates were based on a more extensive set of data on both peak stress and

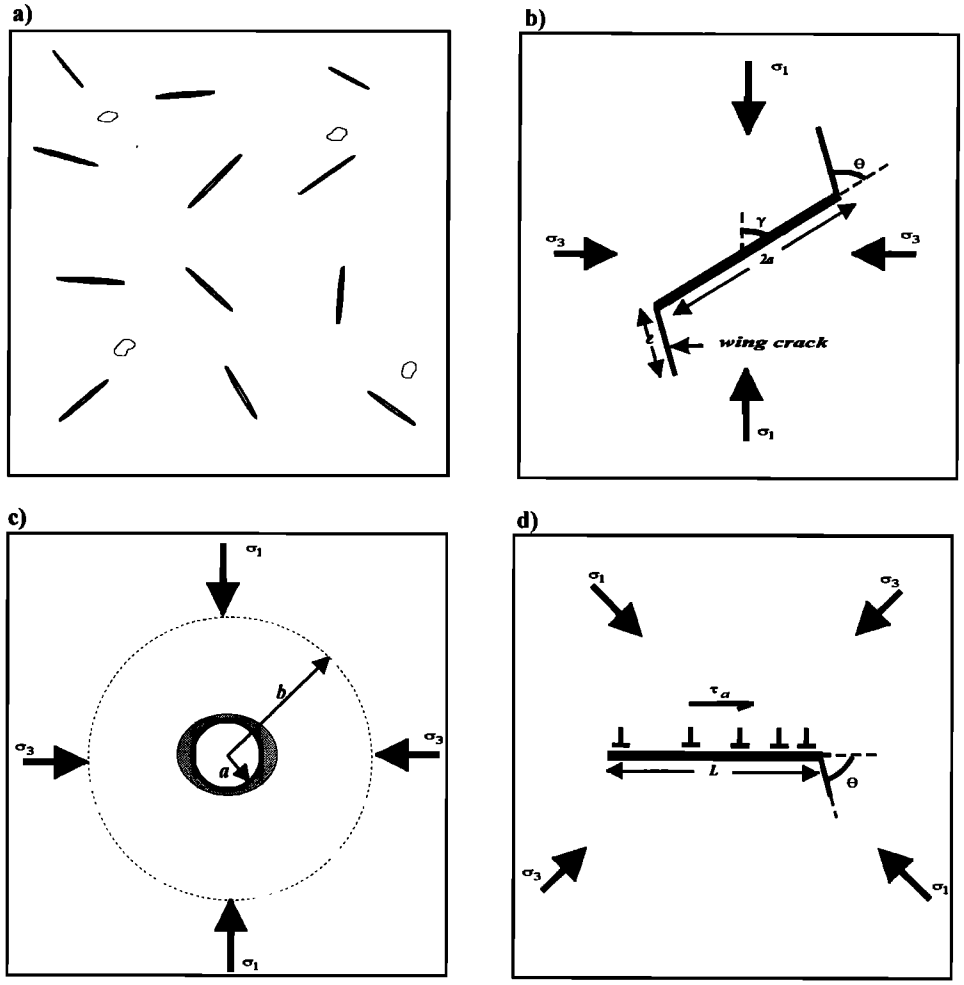

Figure 8. Conceptual models of pore space and three micromechanical processes in Solnhofen limestone. (a) The pore space is composed of microcracks and quasi-spherical pores. (b) The sliding wing crack model is applicable at low confining pressure where dilatancy and brittle fracture were observed. (c) Plastic collapse of isolated spherical pores is responsible for shear-enhanced compaction at relatively high mean stresses. (d) Microcracking induced by dislocation pileup results in the transition from shear-enhanced compaction to dilatant cataclastic flow.

onset of dilatancy of samples from an identical block. *Ashby and Sammis* [1990] choice of preexisting crack length ($2a$ = 50 μm) is ~ 10 times the average grain size of Solnhofen limestone. If we take the more plausible assumption that the sliding crack length is comparable to the average grain size, then $2a \sim 5$ μm and our data suggest that $K_{IC} \sim 0.27$ MPa m$^{1/2}$, which is in reasonable agreement with experimentally determined value for calcite. For example, *Atkinson and Avdis* [1980] reported a value of 0.19 MPa m$^{1/2}$ for crack propagation along the (1011) orientation.

3.4. Onset and Development of Shear-Enhanced Compaction: Plastic Pore Collapse

Two end-members have been developed to model the inelastic compaction of porous rock. For a rock in which crystal plasticity processes (such as mechanical twinning and dislocation slip) initiate at relatively low stress levels, *Curran and Carroll* [1979] modeled the stress-induced compaction that arises from plastic collapse of isolated spherical pores. For a relatively porous rock in which tensile stress concentration can readily be built up at impinging grain contacts, *Zhang et al.* [1990] modeled the pore collapse that arises from grain-scale brittle processes. While this Hertzian fracture model has been demonstrated to be widely applicable to porous siliciclastic rocks [*Wong et al.*, 1997], our mechanical data and preliminary microstructural observations indicate that the plastic pore collapse model is more relevant to compaction in Solnhofen limestone. The compactive yield stresses (Figure 6) are significantly lower than the predictions of the Hertzian fracture model for a siliciclastic rock of porosity and grain size comparable to those of Solnhofen limestone. Furthermore, these stress levels are comparable to levels required for the initiation of dislocation slip in calcite [*Turner et al.*, 1954; *Fredrich et al.*, 1989].

We saw earlier that after closure of the microcrack porosity, the pore space is mainly composed of isolated, quasi-spherical pores. *Curran and Carroll* [1979] considered a dilute concentration of spherical pores, with dimensions sufficiently small that one can model the representative element volume as a thick, concentric spherical shell (Figure 8c) of inner radius a and outer radius b. To relate the local

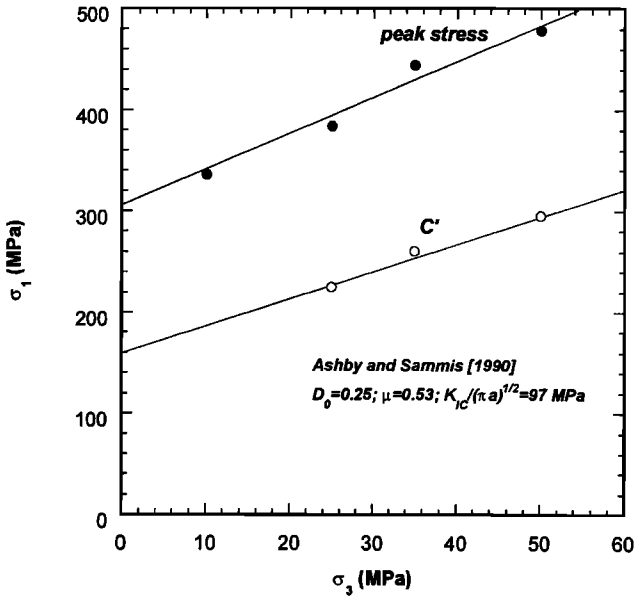

Figure 9. *Ashby and Sammis'* [1990] model was used to interpret our peak stress and onset of dilatancy data at confining pressures of 10, 25, 35, and 50 MPa. The axial stress at the peak is plotted as a function of the confining pressure, and the linear fit is also shown with parameter values as indicated.

geometry to the total porosity ϕ, the radii a and b are chosen such that $\phi = (a/b)^3$.

A Reuss condition is assumed for the local stress state: the outer spherical surface of the representative element volume is subjected to a stress field identical to what is remotely applied to the macroscopic continuum. The applied stress field induces stress concentration in the vicinity of the spherical pore, and plastic flow occurs if the local stress field σ_{ij} satisfies a specified yield condition. In their elastic-plastic model, *Curran and Carroll* [1979] adopted the von Mises yield criterion

$$\sqrt{J_2} = k = Y/\sqrt{3}, \tag{5}$$

where $J_2 = [(\sigma_{11} - \sigma_{22})^2 + (\sigma_{22} - \sigma_{33})^2 + (\sigma_{33} - \sigma_{11})^2]/6 + \sigma_{12}^2 + \sigma_{13}^2 + \sigma_{23}^2$ is the second invariant of the deviatoric stress tensor. The parameters k and Y correspond to the plastic yield stresses for pure shear and uniaxial tension (or compression), respectively. For a porous rock subjected to conventional triaxial compression, plastic yield initiates at the circular perimeter of the spherical pore that is parallel to σ_3 if the remotely applied stresses satisfy this condition:

$$9RP^2 + SP(3P - Q) + (U + V + 3W)(P - Q/3)^2 + 2WPQ = k^2 = Y^2/3, \tag{6}$$

where P is the mean stress $(\sigma_1 + 2\sigma_3)/3$, Q is the differential stress $\sigma_1 - \sigma_3$, and the coefficients R, S, U, V, and W depend on the elastic moduli and the ratio a/b (and therefore the porosity). Although these coefficients were explicitly derived by *Curran and Carroll* [1979], it should be noted that there are several typographical errors in their paper. For the reader's convenience, we have summarized the mathematical development and corrected the errors in the appendix.

If the elastic moduli are specified and the principal stresses are normalized with respect to Y (or k), then a family of yield envelopes can be calculated using equation (6) for different values of initial porosity (Figure 10a). The differential stress at the onset of plastic pore collapse decreases with increasing mean stress and porosity. We have used the Reuss averages

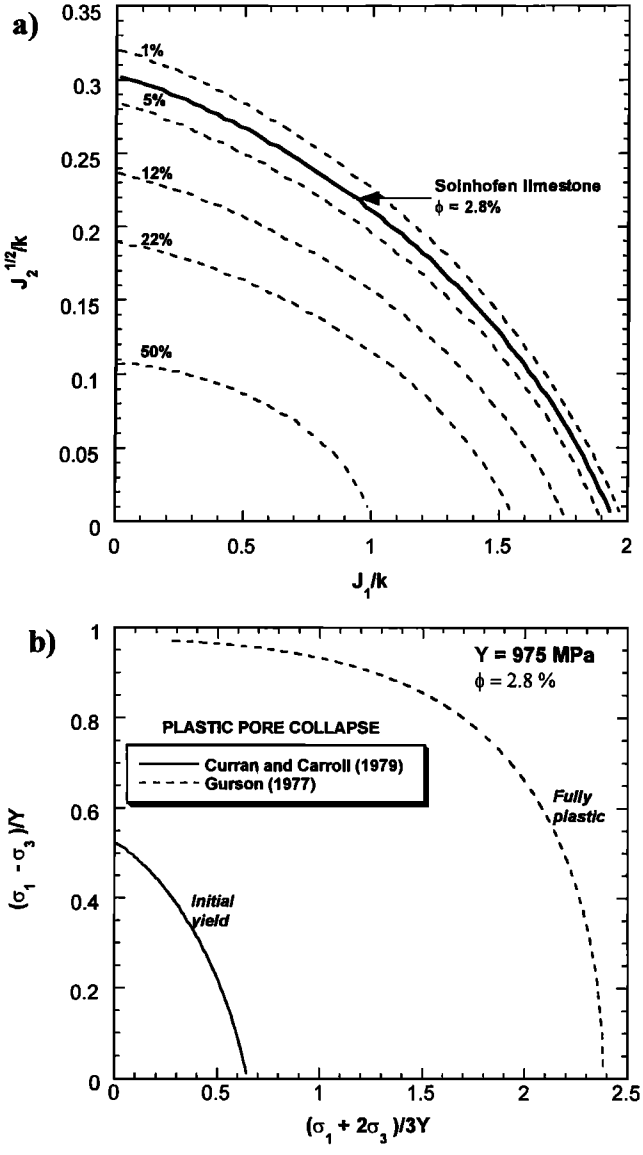

Figure 10. (a) Initial yield surface assuming matrix material governed by von Mises yield criterion calculated using the model of *Curran and Carroll* [1979]. Numbers above curves indicate the porosity. All the curves are calculated with the Reuss averages for elastic moduli of calcite: $K = 7.25 \times 10^5$ MPa and $\mu = 2.69 \times 10^5$ MPa. The solid curve was calculated using the porosity of the Solnhofen limestone after closure of the microcracks (i.e., ϕ = 2.8%). (b) Evolution of the yield surface of Solnhofen limestone with plastic pore collapse: the solid curve is for initial yield calculated using the model of *Curran and Carroll* [1979], and the dashed curve is for total plastic yielding calculated using the model of *Gurson* [1977] with the yield stress Y = 975 MPa.

for the elastic moduli of calcite, but as noted by *Curran and Carroll* [1979], the yield envelope has a relatively weak dependence on the elastic moduli. Except for slight differences in the curvatures, our curves in Figure 10a are nearly the same as theirs calculated using different elastic moduli.

The experimental data for the onset of shear-enhanced compaction (Figure 6) can be fitted with the theoretical yield envelope for plastic pore collapse if an uniaxial yield stress of $k = 563$ MPa (or $Y = 975$ MPa) is assumed (Figure 11). For reference, the critical resolved shear stresses for *f* slip in calcite is 216 MPa, and for *r* slip it ranges from 145 to 185 MPa [*Turner et al.*, 1954; *Griggs et al.*, 1960]. Although our inferred value of k is higher than these yield stresses measured for specific slip systems of calcite, we consider it likely that the macroscopic yield would require a significantly higher stress level. The plastic pore collapse model requires homogeneous plastic flow to occur in the proximity of the pore surface. As elaborated by *Paterson* [1969], the von Mises requirement of five independent slip systems as a necessary condition for this type of macroscopic flow implies that multiple slip systems (some of which are not favorably oriented) need to be activated, and strain hardening would take place very rapidly.

It is well known that *e*-twinning in calcite can be activated at very low stresses. When calcite crystals are favorably oriented for twinning, then the combination of twinning and one of the slip modes would provide the equivalent of five independent slip systems [*Paterson*, 1969, 1979]. Indeed, microstructural observations of *Fredrich et al.* [1989] suggest that fully plastic flow in Carrara marble (at a differential stress of 329 MPa and confining pressure of 300 MPa) can be achieved by the combination of twinning and *r* slip. Our preliminary microstructural observations on a Solnhofen sample deformed in the fully compactive regime (at confining pressure of 435 MPa) indicate that pervasive pore collapse had occurred with somewhat limited twinning activity.

If we focus on the deformation in the vicinity of a pore, then the plastic zone expands with increasing differential stress. The progressive expansion of the plastic zone and the resultant enhancement of compaction were analyzed by *Curran and Carroll* [1979] using finite element simulations. Ultimately, the solid part of the hollow sphere will have yielded completely. Analytic approximations for the stress states at which this final stage occurs were derived by *Green* [1972] and *Gurson* [1977]. According to *Carroll and Carman's* [1985] finite element calculations, *Gurson's* [1977] relation gives better approximation at low porosities. His relation for total plastic yield of a porous sphere can be expressed in terms of the applied mean and differential stresses

$$\left(\frac{Q}{Y}\right)^2 + 2\phi\cosh\left(\frac{3P}{2Y}\right) = (1+\phi^2), \tag{7}$$

where Y is the initial yield stress under uniaxial loading (as defined for equation (5)) and ϕ is the current porosity. It should be noted that the total yield condition does not depend on the elastic moduli or initial porosity. As shown in Figure 10b, the attainment of total yield requires a significant increase of differential stress subsequent to initial yield. Our mechanical data do not suggest that this final stage of plastic pore collapse was achieved in our experiments on Solnhofen limestone.

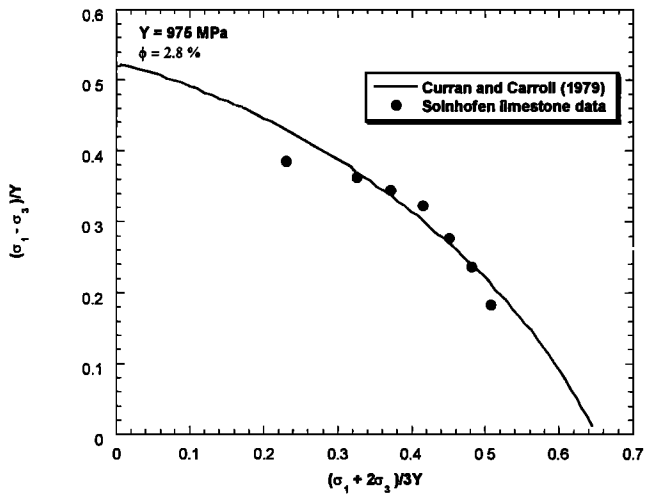

Figure 11. Comparison between experimental data and the model of *Curran and Carroll* [1979], plotted in the *P-Q* space normalized by the yield stress taken as 975 MPa.

3.5. Transition From Shear-Enhanced Compaction to Dilatancy: Microcracking Induced by Dislocation Pileup

The plastic collapse model focuses on the deformation in the vicinity of the quasi-spherical pores. However, as density of the dislocations increases during the strain hardening, their movement is inhibited by obstacles that include grain boundaries, second-phase particles, and nearby dislocations. As a result, a pileup will occur in which mutually repulsive forces between neighboring dislocations are counteracted by the externally applied shear stress (Figure 8d). Microcracking may be induced if the tensile stress concentration ahead of the dislocation pileup is sufficiently high [*Zener*, 1948]. Nucleation and propagation of such microcracks induce the pore space to dilate.

If we consider a slip plane that is subjected to a resolved shear stress τ_a, dislocations can move if this stress exceeds the lattice "friction" stress τ_f. If the dislocations pileup at an obstacle, then the stress concentration ahead of the pile up may nucleate tensile cracking if the stresses satisfy the following condition [*Stroh*, 1957; *Wong*, 1990]:

$$K_{IC} = \frac{4\sqrt{2}}{\sqrt{3\pi}}(\tau_a - \tau_f)\sqrt{L}, \tag{8a}$$

where L is the length of the dislocation pileup. If the rock is under triaxial compression, then the resolved stress attains its maximum value of $\tau_a = (\sigma_1 - \sigma_3)/2$ for a slip plane oriented at 45° to the principal stresses. Hence the crack initiation condition can alternatively be written as

$$\sigma_1 - \sigma_3 = \frac{\sqrt{3\pi}}{2\sqrt{2}}\frac{K_{IC}}{\sqrt{\pi L}} + 2\tau_f. \tag{8b}$$

It is plausible that the dimensions of the dislocation pileup and sliding crack both scale as the grain size, and therefore as

a first approximation, one may take $L \sim 2a$ (Figures 8b and 8d) and use the results from our wing crack analysis to infer that $K_{IC}/(\pi L)^{1/2} \sim 68$ MPa. Substituting this into equation (8b), we see that the first term on the right-hand side is ~187 MPa, which is significantly less than the $\sigma_1 - \sigma_3$ values for $C^{*\prime}$ (Figure 6). Hence equation (8b) requires that the stress τ_f is comparable to the critical resolved shear stress for translational slip in calcite. If indeed τ_f can be approximated by experimentally determined values of the critical resolved shear stresses for the *r* and *f* slip systems [*Turner et al.*, 1954; *Griggs et al.*, 1960], then the $C^{*\prime}$ data are bracketed by theoretical estimates from equation (8b) (shown as solid lines in Figure 12).

The apparent agreement suggests that the interplay of dislocation and microcracking activities can explain the transition from shear-enhanced compaction to dilatancy. However, it should be noted that such a comparison has certain limitations. First, the shear stress τ_f as originally envisioned by *Stroh* [1957] represents the lattice friction stress, which is probably very small in calcite. Hence the relatively high values here should be interpreted as generalized resistance stresses that include lattice friction as well as other stresses that result from complex interactions with various obstacles present in the polycrystalline aggregate. Second, the model is for the initiation of dilatant cracking, but the overall development of dilatancy in the rock as a whole would require the cumulative dilation due to cracking exceed the concomitant compaction due to plastic pore collapse. Hence equation (8b) only provides a lower bound on the critical stress at the transition from shear-enhanced compaction to dilatancy, which probably occurs after the cracks have propagated over certain distances. Third, the data suggest a slight dependence of $C^{*\prime}$ on pressure, whereas the model predicts that the differential stress level is pressure-independent (equation (8b)). As elaborated by

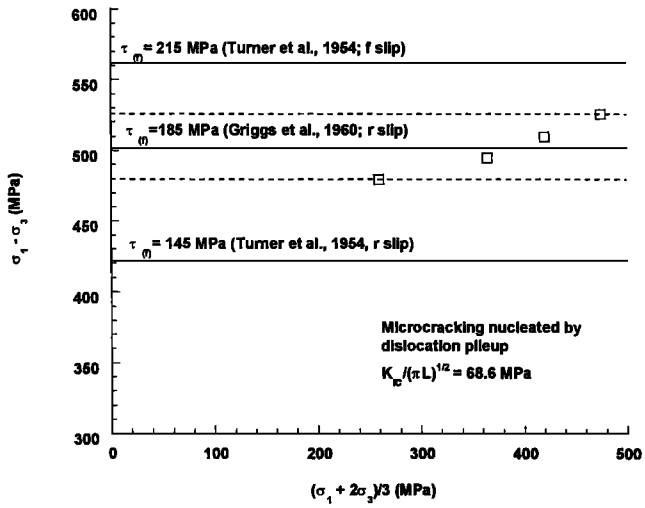

Figure 12. Predicted values of differential stress for the nucleation of tensile crack induced by dislocation pileup (solid lines). For reference, experimentally determined values for *r* slip and *f* slip systems in calcite [*Turner et al.*, 1954; *Griggs et al.*, 1960] are also shown. For comparison, the critical stresses $C^{*\prime}$ for the transition from shear-enhanced compaction to dilatant cataclastic flow are plotted in the *P-Q* space.

Francois and Wilshaw [1968] and *Wong* [1990], the extension of a crack nucleated by dislocation pileup is sensitively dependent on pressure, even though the nucleation process itself is pressure-independent. Last, our preliminary microstructural observations of a sample deformed to beyond $C^{*\prime}$ (at the confining pressure of 200 MPa) indicate extensive microcracking, as well as mechanical twinning, and therefore the interplay with dislocation, microcracking, and twinning activities should be integrated in future refinement of the micromechanical model.

3.6. Effect of Porosity and Grain Size on the Brittle-Ductile Transition

We have focused on porosity change and failure mode as two key aspects of the phenomenology of the brittle-ductile transition. A comparison of the Solnhofen limestone (Figure 6) and Lance sandstone (Figure 7) shows that the phenomenological behaviors in these two rocks of intermediate porosities are qualitatively similar. In each case the brittle-ductile transition is associated with a complex interplay of dilatant and compactive deformation mechanisms. While these similarities underscore the important control that porosity exerts on the phenomenology of the brittle-ductile transition, it should also be kept in mind that the micromechanical processes are actually very different in the silicate and calcite rocks.

While dilatancy and compaction in silicate rocks arise from various modes of grain-scale cracking operative at room temperature, our micromechanical analyses emphasize the importance of crystal plasticity as well as microcracking mechanisms in the limestone. The same mechanisms are activated in calcite rocks of different porosities and grains sizes to result in fundamentally different failure modes. This complex connection between micromechanics and macroscopic failure mode can be illustrated by comparison of Solnhofen limestone with Carrara marble.

Figure 13 summarizes the critical stresses and failure modes of the relatively compact Carrara marble [*Fredrich et al.*, 1989]. On the one hand, the overall behavior in the brittle faulting regime is qualitatively similar in Carrara marble and the more porous Solnhofen limestone. Applying equations (2) and (4) to data of *Fredrich et al.* [1989] on onset of dilatancy and peak stress, we obtained values of $\mu = 0.55$, $K_{IC}/(\pi a)^{1/2} = 27$ MPa and $D_0 = 0.3$ for Carrara marble. As expected the friction coefficients in the limestone and marble are similar. The fracture toughness parameter $K_{IC}/(\pi a)^{1/2}$ is significantly lower in coarse-grained Carrara marble possibly because the crack length *a* is expected to scale with grain size. Such effects of grain size on strength and brittle-ductile transition have been discussed in some detail by *Fredrich et al.* [1990]. While the wing crack model may idealize the complicated mechanisms that are actually involved in brittle faulting, it provides a semiquantitative description that is particularly useful for a comparative analysis. It should also be noted that porosity also has influence on the brittle strength. In Figure 14 we compile all the published data for Solnhofen limestone (with initial porosities ranging from 1.7% to 5.9%). There is a general trend for the peak stress to decrease with increasing porosity.

On the other hand, two significant differences between the marble and limestone were observed in the cataclastic flow regime. First, inelastic compaction was absent, and only

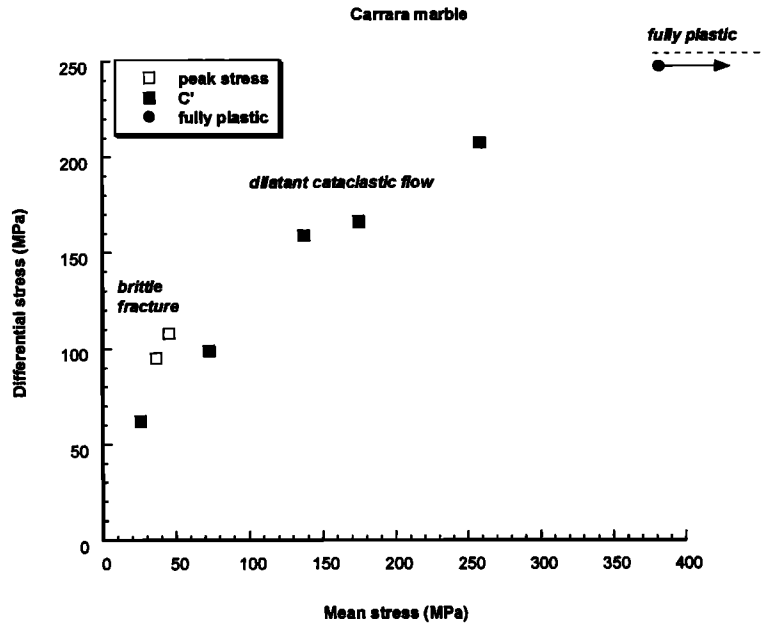

Figure 13. Stress state at the onset of dilatancy C' (in both brittle faulting and cataclastic flow regimes) and brittle strength are shown in the P-Q space for data on Carrara marble from *Fredrich et al.* [1989].

dilatancy was observed in the relatively compact Carrara marble. As documented by *Fredrich et al.* [1989], dilatant cataclastic flow in Carrara marble is manifested by mechanical twinning and dislocation slip that may promote or inhibit microcracking at different stress and pressure conditions. While these crystal plasticity processes induce local tensile stress concentration that nucleate wing cracks, twin and slip bands may also act as barriers that arrest microcrack propagation. In Solnhofen limestone our preliminary microstructural observations indicate that the role of twinning seems to be secondary, especially in samples that had undergone plastic pore collapse. This is in agreement with *Rowe and Rutter's* [1990] observation that a relatively high stress (~300 MPa) is required to activate twinning in this fine-grained limestone. Mechanical twinning arises from the homogeneous shear of successive planes of atoms that causes one portion of the lattice to become a mirror image of the other. The nature of the twinning process is such that it is confined within a single grain. Consequently, the local tensile stress concentration at the tip of a twin band should scale with the spatial extent of the shear strain (and therefore the dimensions of the twin band and grain size), and therefore wing crack nucleation or crack arrest is less likely to be induced by twinning activity in the relatively fine-grained Solnhofen limestone.

Second, Carrara marble (Figure 13) underwent a transition to fully plastic flow (with negligible volume change) at a stress level of 329 MPa (at a confining pressure 300 MPa) that is significantly lower than our inferred value of Y (~975 MPa) for Solnhofen limestone. In Carrara marble, fully plastic flow involves the cooperative mechanisms of mechanical twinning and dislocation slip [*Fredrich et al.*, 1989]. In contrast, the role of mechanical twinning is relatively limited in Solnhofen limestone, and therefore plastic flow hinges on the activation of multiple dislocation slip systems that require a significantly higher stress level [*Paterson*, 1969]. More systematic microstructural observations using the optical and transmission electron microscopes should be pursued to elucidate this question.

4. Conclusion

In this study, we have demonstrated that shear-enhanced compaction and pore collapse are readily observed in the Solnhofen limestone that has an initial porosity as low as 3% and pore size of the order of 10 μm. As a function of pressure, three primary failure modes were identified in this relatively compact limestone. At relatively low pressures (≤ 50 MPa), dilatancy was observed as a precursor to the occurrence of brittle faulting. At relatively high pressures (≥ 350 MPa) the samples failed by cataclastic flow associated with shear-enhanced compaction and strain hardening. At intermediate pressures, shear-enhanced compaction was observed during the initial stage of strain hardening but only as a transient precursor that ultimately led to dilatant cataclastic flow. This intriguing phenomenon implies that stress-induced compaction and dilatancy should not be viewed as mutually exclusive processes, especially when large strains are involved.

Several theoretical models were employed to interpret the micromechanics of the brittle-ductile transition in Solnhofen limestone. Comparison of our data with results for siliciclastic rocks underscores that since crystal plasticity of the calcite grains has a predominant role in limestone, the Hertzian fracture model is not appropriate for analyzing the compaction phenomena. Our laboratory data on the onset of shear-enhanced compaction are in reasonable agreement with *Curran and Carroll's* [1979] plastic pore collapse model if a relatively high yield stress of Y= 975 MPa is assumed. In the transitional regime the *Stroh* [1957] model for microcrack nucleation due to dislocation pileup can be used to analyze the transition from shear-enhanced compaction to dilatancy.

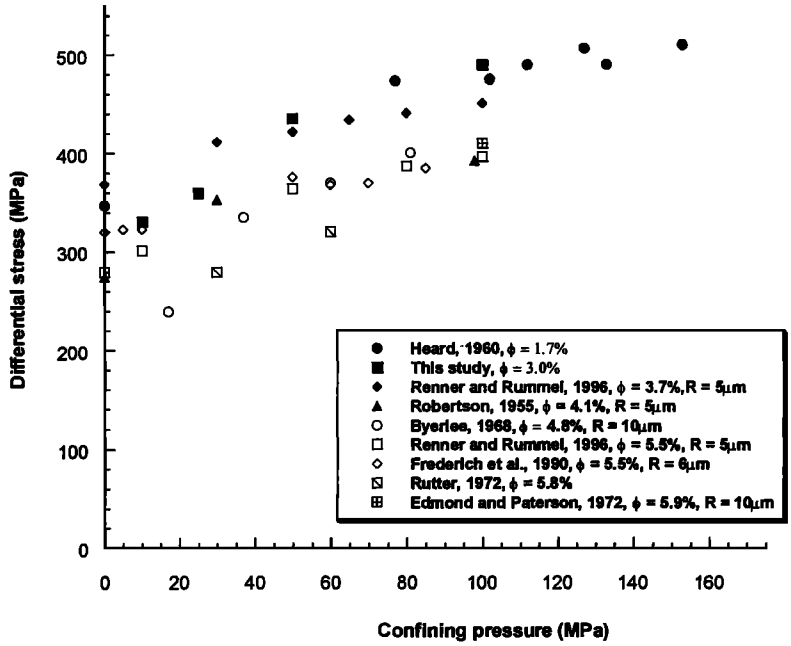

Figure 14. Compilation of peak stress data for Solnhofen limestones of different porosities and grain sizes.

In the brittle faulting regime the wing crack model provides a consistent description of the effect of grain size on the onset of dilatancy and brittle faulting in Solnhofen limestone and Carrara marble.

Appendix: Initiation of Plastic Collapse of a Spherical Pore Induced by Triaxial Compression

Following *Curran and Carroll* [1979], we consider a hollow sphere of homogeneous, isotropic material. The spherical shell has inner and outer radii a and b, respectively, and it is subject to the following boundary conditions: (1) the inner boundary is traction free and (2) on the outer boundary, the traction is given by $t_i = T_{ij} n_j$, where n_j is the outward unit normal to the outer surface of the sphere, and the applied stress is $T_{11} = \sigma_1$, $T_{22} = \sigma_3$, $T_{33} = \sigma_3$, with all the off-diagonal elements being zero.

The material response is elastic-plastic. Before the onset of plastic yield, the solid part of the sphere is isotropic and linearly elastic, with moduli given by the two Lamé constants λ and μ. *Curran and Carroll* [1979] considered the initial plastic yield to obey the Drucker-Prager criterion, which depends on the mean and deviatoric stresses. Here we focus on plastic yield due to crystal plasticity that is pressure-independent. Hence the Drucker-Prager criterion reduces to the von Mises criterion: $J_2^{1/2} = k$ as defined in equation (5) of the text. For our case, plastic yield initiates at the circular perimeter of the spherical pore (on the X_1-X_2 plane) when the applied stresses satisfy this condition:

$$\left\{R(\sigma_1 + 2\sigma_3)^2 + S\sigma_3(\sigma_1 + 2\sigma_3) + U\sigma_3^2 + V\sigma_3^2 + W(\sigma_1^2 + 2\sigma_3^2)\right\}^{1/2} = k \tag{A1}$$

with the parameters R, S, U, V, and W are defined by

$$R = \frac{2}{3}\mu^2\left(2A'^2a^2 - 2A'Ca - C^2\right) \tag{A2a}$$

$$S = \frac{2}{3}\mu^2 a^2\left(8A'Ba - 4BC + 4A'B'a^2 - 2B'Ca + 4A'C' - \frac{2CC'}{a} + \frac{6A'C}{a}\right) \tag{A2b}$$

$$U = \frac{2}{3}\mu^2 a^4\left(2B^2 + 8BB'a + \frac{2BC'}{a} + 2B'^2a^2 + 4B'C' + \frac{C'^2}{2a^2} + \frac{6B'C}{a}\right) \tag{A2c}$$

$$V = \frac{2}{3}\mu^2 a^2\left(6B^2a^2 + 6BC'a + \frac{3}{2}C'^2 + 12BC + \frac{6CC'}{a}\right) \tag{A2d}$$

$$W = 2\mu^2C^2 \tag{A2e}$$

The primed symbol indicates differentiation with respect to the radial distance r, and the functions A, B, and C are given by

$$A(r) = -\frac{D_2}{5r^5} + \frac{D_3\lambda r^2}{(2\lambda + 7\mu)} + \frac{D_5}{r^3} + D_6 \tag{A3a}$$

$$B(r) = \frac{D_1}{r^5} + \frac{D_2}{r^7} + D_3 \tag{A3b}$$

$$C(r) = \frac{2\mu D_1}{3(\lambda + \mu)r^3} - \frac{2D_2}{5r^5} - \frac{(5\lambda + 7\mu)}{(2\lambda + 7\mu)}D_3r^2 + D_4 \tag{A3c}$$

in which the parameters D_1, D_2, D_3, D_4, D_5 and D_6 are in turn defined by

$$D_1 = \frac{16\mu(19\lambda+14\mu)(b^7-a^7)}{(2\lambda+7\mu)a^7b^7\Delta} \tag{A4a}$$

$$D_2 = -\frac{16\mu(19\lambda+14\mu)(b^5-a^5)}{(2\lambda+7\mu)a^5b^5\Delta} \tag{A4b}$$

$$D_3 = \frac{128\mu(b^2-a^2)}{a^7b^7\Delta} \tag{A4c}$$

$$D_4 = \frac{16\mu}{15(2\lambda+7\mu)(\lambda+\mu)\Delta}\left[\frac{1}{a^{10}}\left(171\lambda^2+392\mu\lambda+196\mu^2\right)\right.$$
$$+\frac{504}{a^5b^5}\left(\lambda^2+2\lambda\mu+\mu^2\right)$$
$$\left.-\frac{25}{a^3b^7}\left(27\lambda^2+56\mu\lambda+28\mu^2\right)\right] \tag{A4d}$$

$$D_5 = \frac{\lambda D_1}{6(\lambda+\mu)}+\frac{2D_2(b^5-a^5)}{5a^2b^2(b^3-a^3)}$$
$$+\frac{\lambda D_3 a^3b^3(b^2-a^2)}{4(2\lambda+7\mu)(b^3-a^3)} \tag{A4e}$$

$$D_6 = \frac{1}{(3\lambda+2\mu)}\left[\frac{8\mu D_2}{5a^2b^2}\frac{(b^2-a^2)}{(b^3-a^3)}\right.$$
$$\left.+\frac{\lambda\mu D_3}{(2\lambda+7\mu)}\frac{(b^5-a^5)}{(b^3-a^3)}-\lambda D_4\right] \tag{A4f}$$

with

$$\Delta = \frac{32\mu^2}{15(2\lambda+7\mu)(\lambda+\mu)a^{10}b^{10}}\left[\left(b^{10}+a^{10}\right)\left(171\lambda^2+392\mu\lambda\right.\right.$$
$$\left.+196\mu^2\right)+1008a^5b^5\left(\lambda^2+2\mu\lambda+\mu^2\right)$$
$$\left.-25\left(a^7b^3+a^3b^7\right)\left(27\lambda^2+56\mu\lambda+28\mu^2\right)\right.$$

Acknowledgments. We are grateful to Dave Olgaard for providing the block of Solnhofen limestone. Preliminary microstructural observations on deformed samples were conducted by Veronika Vajdova. We have benefited from discussions with Joanne Fredrich and Mervyn Paterson. Constructive and insightful reviews were provided by Georg Dresen and Ernie Rutter, as well as the Associate Editor Douglas Schmitt. The second author's exchange visit to Stony Brook was sponsored by the Magistère Interuniversitaire de Sciences de la Terre at the Ecole Normale Supérieure, Paris. The micromechanical modeling was initiated when the third author was a visiting professor at the Ecole Normale Supérieure. He would like to thank Yves Guéguen for the hospitality and many useful discussions on this topic. This research was partially supported by the Office of Basic Energy Sciences, Department of Energy, under grants DE-FG-02-94ER14455 and DE-FG02-99ER14996.

References

Ashby, M.F., and C.G. Sammis, The damage mechanics of brittle solids in compression, *Pure Appl. Geophys.*, *133*, 489-521, 1990.

Atkinson, B.K., and V. Advis, Fracture mechanics parameters of some rock-forming minerals determined using an indentation technique, *Int. J. Rock Mech. Min. Sci. Geomech. Abstr.*, *17*, 383-386, 1980.

Brace, W.F., Volume changes during fracture and frictional sliding: A review, *Pure Appl. Geophys.*, *116*, 603-614, 1978.

Byerlee, J.D., Brittle-ductile transition in rocks, *J. Geophys. Res.*, *73*, 4741-4750, 1968.

Carroll, M.M., and R.A. Carman, Discussion of Influence of yield surface curvature on flow localization in dilatant plasticity, by M. E. Mear, and J. W. Hutchinson, *Mech. Mat.*, *4*, 409-415, 1985.

Cotterell, B., and J.R. Rice, Slightly curved or kinked cracks, *Int. J. Fract.*, *16*, 155-169, 1980.

Curran, J.H., and M.M. Carroll, Shear stress enhancement of void compaction, *J. Geophys. Res.*, *84*, 1105-1112, 1979.

Drucker, D.C., and W. Prager, Soil mechanics and plastic analysis of limit design, *Q. Appl. Math.*, *10*, 157-165, 1952.

Edmond, J.M., and M.S. Paterson, Volume changes during the deformation of rocks at high pressure, *Int. J. Rock Mech. Min. Sci. Geomech. Abstr.*, *9*, 161-182, 1972.

Fisher, G.J., and M.S. Paterson, Dilatancy during rock deformation at high temperatures and pressures, *J. Geophys. Res.*, *94*, 17,607-17,617, 1989.

Fossum, A.F., P.E. Senseny, T.W. Pfeifle, and K.D. Mellegard, Experimental determination of probability distributions for parameters of a salem limestone cap plasticity model, *Mech. Mat.*, *21*, 119-137, 1995.

Francois, D., and T.R. Wilshaw, The effect of hydrostatic pressure on the cleavage fracture of polycrystalline materials, *J. Appl. Phys.*, *39*, 4170-4177, 1968.

Fredrich, J.T., B. Evans, and T.-f. Wong, Micromechanics of the brittle to plastic transition in Carrara marble, *J. Geophys. Res.*, *94*, 4129-4145, 1989.

Fredrich, J.T., B. Evans, and T.-f. Wong, Effect of grain size on brittle and semi-brittle strength: Implications for micromechanical modeling of failure in compression, *J. Geophys. Res.*, *95*, 10,907-10,920, 1990.

Green, R.J., A plasticity theory for porous solids, *Int. J. Mech. Sci.*, *14*, 215, 1972.

Griggs, D.T., F.J. Turner, and H.C. Heard, Deformation of rocks at 500° to 800°, in *Rock Deformation*, edited by D. T. Griggs and J. Handin, *Mem. Geol. Soc. Am.*, *79*, 39-104, 1960.

Gurson, A.L., Continuum theory of ductile rupture by void nucleation and growth, part I, Yield criteria and flow rules for porous ductile media, *J Eng. Mater. Technol.*, *99*, 2-15, 1977.

Hadizadeh, J., and, E.H. Rutter, The low temperature brittle-ductile transition in a quartzite and the occurrence of cataclastic flow in nature, *Geol. Rundsch.*, *72*, 493-509, 1983.

Handin, J., and R.V. Hager, Experimental deformation of sedimentary rocks under confining pressure: Tests at room temperature on dry sample, *Am. Assoc. Pet. Geol. Bull.*, *41*, 1-50, 1957.

Heard, H.C., Transition from brittle fracture to ductile flow in Solnhofen limestone as a function of temperature, confining pressure and interstitial fluid pressure, in *Rock Deformation*, edited by D.T. Griggs and J. Handin, *Mem. Geol. Soc. Am.*, *79*, 193-226, 1960.

Hirth, G., and J. Tullis, The brittle-plastic transition in experimentally deformed quartz aggregates, *J. Geophys. Res.*, *99*, 11,731-11,748, 1994.

Horii, H., and S. Nemat-Nasser, Brittle failure in compression: Splitting, faulting and brittle-ductile transition. *Philos. Trans. Royal Soc. London, Ser. A*, *319*, 337-374, 1986.

Kemeny, J.M., and N.G.W. Cook, Micromechanics of deformation in rocks, in *Toughening Mechanisms in Quasi-Brittle Materials*,

edited by S.P. Shah, Kluwer Acad., pp. 155-188, Norwell Mass., 1991.

Paterson, M.S., Experimental deformation and faulting in Wombeyan marble, *Geol. Soc. Am. Bull., 69*, 465-476, 1958.

Paterson, M.S., The ductility of rocks, in *Physics of Strength and Plasticity*, edited by A.S. Argon, pp. 377-392, MIT Press, Cambridge, Mass., 1969.

Paterson, M.S., *Experimental Rock Deformation: The Brittle Field*, Springer-Verlag, New York, 1978.

Paterson, M.S., Deformation mechanisms in carbonate crystals, in *Physics of Materials, A Festschrift for Dr. Walter Boas*, edited by D.W. Borland, L.M. Clarebrough, and A.J.W. Moore, pp. 199-208, CSIRO and Depart. of Metall., Univ. of Melbourne, Melbourne, Victoria, 1979.

Renner, J., and F. Rummel, The effect of experimental and microstructural parameters on the transition from brittle failure to cataclastic flow of carbonate rocks, *Tectonophysics, 258*, 151-169, 1996.

Robertson, E.C., Experimental study of the strength of rocks, *Geol. Soc. Am. Bull., 66*, 1275-1314, 1955.

Rowe, K.J., and E.H. Rutter, Palaeostress estimation using calcite twinning: Experimental calibration and application to nature, *J. Struct. Geol., 12*, 1-17,1990.

Rutter, E.H., The effects of strain-rate changes on the strength and ductility of Solnhofen limestone at low temperature and confining pressures, *Int. J. Rock Mech. Min. Sci. Geomech. Abstr., 9*, 183-189, 1972.

Rutter, E.H., The influence of temperature, strain rate and interstitial water in the experimental deformation of calcite rocks, *Tectonophysics, 22*, 331-334, 1974.

Schmid, S.M., J.N. Boland, and M.S. Paterson, Superplastic flow in fine grained limestone, *Tectonophysics, 43*, 257-291, 1977.

Schock, R.N., H.C. Heard, and D.R. Stephens, Stress-strain behavior of a granodiorite and two graywackes on compression to 20 kilobars, *J. Geophys. Res., 78*, 5922-5941, 1973.

Shimada, M., Mechanism of deformation in a dry porous basalt at high pressures, *Tectonophysics, 121*, 153-173, 1986.

Shimada, M., A. Cho, and H. Yukatake, Fracture strength of dry silicate rocks at high confining pressures and activity of acoustic emission, *Tectonophysics, 96*, 159-172, 1983.

Simmons, G., and H.F. Wang, *Single Crystal Elastic Constants and Calculated Aggregate Properties*, MIT Press, Cambridge, Mass., 1971.

Stroh, A.N., A theory of the fracture of metals, *Adv. Phys., 6*, 418-465, 1957.

Tapponier, P., and, W.F. Brace, Development of stress-induced microcracks in Westerly granite, *Int. J. Rock Mech. Min. Sci. Geomech. Abstr., 13*, 103-112, 1976.

Teufel, L.W., D.W. Rhett, and H.E. Farrell, Effect of reservoir depletion and pore pressure drawdown on in situ stress and deformation in the Ekofisk field, North Sea, *Proc. U.S. Rock Mech. Symp., 32*, 63-72, 1991.

Tullis, J., and R.A. Yund, The brittle-ductile transition in feldspar aggregates: An experimental study, in *Fault Mechanics and Transport Properties of Rocks*, edited by B. Evans and T.-f. Wong, pp. 89-117, Academic, San Diego, Calif., 1992.

Turner, F.J., D.T. Griggs, and H.C. Heard, Experimental deformation of calcite crystals, *Geol. Soc. Am. Bull., 65*, 883-934, 1954.

Walsh, J.B., The effects of cracks on the compressibility of rock, *J. Geophys. Res., 70*, 381-389, 1965.

Walsh, J.B., and W.F Brace, Elasticity of rock: A review of some recent theoretical studies, *Rock Mech. Engin. Geol., 4*, 283-297, 1966.

Wong, T.-f., Micromechanics of faulting in Westerly granite, *Int. J. Rock Mech. Min. Sci. Geomech. Abstr., 19*, 49-64, 1982.

Wong, T.-f., Mechanical compaction and the brittle-ductile transition in porous sandstones, in *Deformation Mechanisms, Rheology and Tectonics*, edited by R.J. Knipe and R.H Rutter, *Geol. Soc. Spec. Publ., 54*, 111-112, 1990.

Wong, T-f., C. David, and W. Zhu, The transition from brittle faulting to cataclastic flow in porous sandstones: Mechanical deformation, *J. Geophys. Res., 102*, 3009-3025, 1997.

Zener, C., The micro-mechanism of fracture, in *Fracture of Metals*, edited by F. Johnson, W.P. Roop, and R.T. Bayles, pp. 3-31, Am. Soc. for Metals, Cleveland, Ohio, 1948.

Zhang, J., T.-f. Wong, and D.M. Davis, Micromechanics of pressure induced grain crushing in porous rocks, *J. Geophys. Res., 95*, 341-352, 1990.

Zhu, W., and T.-f. Wong, The transition from brittle faulting to cataclastic flow in porous sandstones: Permeability evolution. *J. Geophys. Res., 102*, 3027-3041, 1997.

P. Baud and T.-f. Wong, Department of Geosciences, State University of New York at Stony Brook, Stony Brook, NY, 11794-2100. (baud@horizon.ess.sunysb.edu; tfwong@notes.cc.sunysb.edu)

A. Schubnel, Département Terre, Atmosphère et Océan, Ecole Normale Supérieure, 24 rue Lhomond, F-75231 Paris cedex 05, France.

(Received June 2, 1999; revised February 15, 2000; accepted April 12, 2000.)